A New Technique for the Photospheric Driving of Non-Potential Solar Coronal Magnetic Field Simulations

Marion Weinzierl

Department of Mathematical Sciences, Durham University
South Road, Durham DH1 3LE, UK

marion.weinzierl@durham.ac.uk

Anthony R. Yeates

Department of Mathematical Sciences, Durham University
South Road, Durham DH1 3LE, UK

Duncan H. Mackay

School of Mathematics and Statistics, University of St. Andrews
North Haugh, St. Andrews, Fife KY16 9SS, Scotland

Carl J. Henney

Air Force Research Lab/Space Vehicles Directorate
3550 Aberdeen Ave. SE, Kirtland AFB, NM, USA
and

C. Nick Arge

Air Force Research Lab/Space Vehicles Directorate
3550 Aberdeen Ave. SE, Kirtland AFB, NM, USA

ABSTRACT

A new technique for driving global non-potential simulations of the Sun's coronal magnetic field solely from sequences of radial magnetic maps of the solar photosphere is developed in this paper. A primary challenge to driving such global simulations is that the required horizontal electric field cannot be uniquely determined from such maps. We show that an "inductive" electric field solution similar to that used by previous authors successfully reproduces specific features of the coronal field evolution in both single and multiple bipole simulations. For these cases the true solution is known because the electric field was generated from a surface flux transport model. The match for these cases is further improved by including the non-inductive electric field contribution from surface differential rotation. Then, using this reconstruction method for the electric field, we show that a coronal non-potential simulation can be successfully driven from a sequence of ADAPT maps of the photospheric radial field, without including additional physical observations which are not routinely available.

Subject headings: magnetohydrodynamics (MHD), Sun: corona, Sun: coronal mass ejections (CMEs), Sun: magnetic fields

1. INTRODUCTION

Non-potential solar coronal magnetic field simulations using the magnetofrictional (MF) method (Yang et al. 1986) have been demonstrated to be a practical alternative to global magnetohydrodynamic (MHD) simulations in long term computationally expensive coronal studies (see, e.g., Yeates 2014). By allowing for the build-up of electric currents and free magnetic energy, the MF method can better approximate physical processes in the corona compared to potential-field source-surface (PFSS) extrapolations. Such non-potential fields have benefits to solar-wind and space-weather forecasting (Edwards et al. 2015).

Similar to full MHD simulations, global MF simulations of the coronal magnetic field require E_θ, E_ϕ as inner boundary conditions on the photosphere. In MHD, this horizontal electric field $\mathbf{E}_\perp$ depends on the vector plasma velocity $\mathbf{v}$, the vector magnetic field $\mathbf{B}$, and a non-ideal dissipation term. Since complete observations of these quantities are not routinely available, previous authors (cf. Amari et al. 2003; Fisher et al. 2010; Mackay et al. 2011; Yang et al. 2012; Cheung & DeRosa 2012; Kazachenko et al. 2014) have shown how this boundary electric field can be inferred from line-of-sight magnetograms to drive both MHD and MF simulations.

In this paper we present MF simulations. However, the photospheric boundary motions are very slow compared to the coronal Alfvén speed, and the plasma beta is low. As a result, for both MHD simulations and MF simulations we would expect the coronal magnetic field evolution to closely approximate a sequence of quasi-steady force-free states. Under these approximations the MHD approach and MF approach produce very similar results. If we are interested primarily in the long-lived structure of the magnetic field rather than the high-frequency dynamics of MHD waves, then the MF method captures the essential evolution more efficiently.

In the case of MF simulations, published results using $\mathbf{E}_\perp$ determined solely from observed magnetogram sequences have been limited to simulations of individual active regions (Mackay et al. 2011; Cheung & DeRosa 2012; Gibb et al. 2014). Global simulations, on the other hand, have used specified velocity and dissipation terms to determine $\mathbf{E}_\perp$ through flux transport models (Mackay & Yeates 2012). In this work, for the first time we explore the driving of global MF simulations directly from sequences of $B_r(\theta, \phi, t)$ maps of the whole solar surface, rather than from a flux transport model. Since we currently have no observed magnetograms of the far-side of the Sun, these maps must have been based partly on modelling to determine how B_r evolves in the unobserved regions (cf. Schrijver & DeRosa 2003; Arge et al. 2010; Henney et al. 2012; Upton & Hathaway 2014). For this paper, we assume that the sequence of maps has already been constructed.

A particular challenge of applying this technique is the non-uniqueness of $\mathbf{E}_\perp$ (cf. Fisher et al. 2010). This is discussed further in Sec. 4, and essentially reduces to the question of how to approximate the "non-inductive" component of $\mathbf{E}_\perp$. This is the curl-free component that cannot (in principle) be deduced purely from observations of $\mathbf{B}$. In this paper, we illustrate two different approaches for reconstructing $\mathbf{E}_\perp$ with: (i) the non-inductive component is simply neglected (i.e., the simplest solution); (ii) the dominant non-inductive contribution is assumed to come from advection by solar differential rotation, for which the appropriate correction may be computed.

We demonstrate our approaches for estimating $\mathbf{E}_\perp$ through three different cases. First, we simulate the decay of a single bipolar active region in a low background magnetic field. Second, we apply our reconstruction approaches to a full Sun $B_r(\theta, \phi, t)$ sequence containing multiple evolving bipolar regions. These two sequences of maps are taken from our own surface flux transport simulations, allowing us to compare the reconstructed electric field with the known electric field from the original simulation. Third, in order to demonstrate the applicability of this method to deal with real observational data, we show how our global non-potential coronal magnetic field simulation can be driven by Air Force Data Assimilative Photospheric Flux Transport (ADAPT) maps (Arge et al. 2010; Henney et al. 2012; Hickmann et al. 2015). This poses additional challenges to the method, as new observational data are integrated into these maps when they become available, which produces a time discontinuity that has a non-negligible effect on the simulation (see Sec. 5.3).

Although we begin with tests based on flux transport simulations, where $\mathbf{E}_\perp$ is known, the technique we are developing has much wider applicability. The standard flux transport model (Section 3.1) has three main components: two advection velocities (meridional flow and differential rotation) and a macroscopic diffusion term. Whilst the advection acts over all spatial scales, the diffusion is designed to represent the net effect of the random walk of many small convective cells dispersing magnetic flux over the solar surface, thus limiting the standard flux transport model to spatial scales larger than that of the supergranulation. Under these approximations, the flux transport model successfully models the evolution of the global magnetic field and the dispersal of flux out of active regions. It cannot however model the complex small scale dynamics that occur within active regions. Nor can it account for localised variations in the solar surface flows. By developing a technique to drive MF simulations from arbitrary sequences of magnetic maps, we aim to circumvent these limitations. Although we begin by validating against the standard flux transport model, future simulations will be limited only by the spatial resolution of observations and the computing power available.

This paper is organized as follows. The non-potential coronal model we use is described in Section 2, and the three cases of input B_r maps simulated are described in Section 3. Our methods for electric field inversion are described in Section 4, and the resulting non-potential simulations are discussed in Section 5.

2. NON-POTENTIAL CORONAL MODEL

The magnetofrictional (MF) technique follows the evolution of the large-scale magnetic field in the solar corona. Instead of solving the full MHD momentum equation, the velocity $\mathbf{v}$ is approximated by the magneto-frictional form introduced by Yang et al. (1986), namely

$$\mathbf{v} = \nu^{-1}(\mathbf{J} \times \mathbf{B}/B^2) \qquad (1)$$

where $\mathbf{J} = \nabla \times \mathbf{B}$ and ν is a friction coefficient. This form enforces the relaxation of the magnetic field towards a nonlinear force-free state where $\mathbf{J} \times \mathbf{B} = 0$. The MF model allows for a gradual
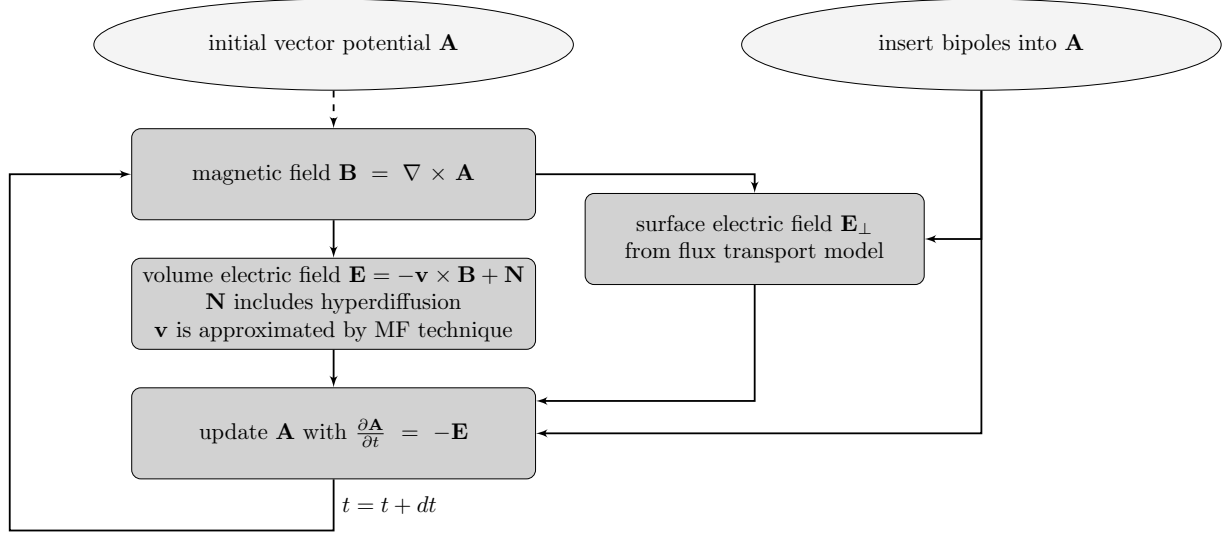
build-up and conservation of magnetic energy and electric currents in the corona, in contrast to common extrapolation methods, which have no memory of magnetic connectivity.

The two flowcharts in Figure 1 indicate how the non-potential magnetic field is evolved over time, contrasting previous flux-transport driven simulations (Figure 1a) with the new simulations described in this paper (Figure 1b). In both cases, the vector potential $\mathbf{A}$ in the coronal volume is evolved through the same MF technique, and the time stepping is done using the Euler method. The difference lies in how the lower boundary condition for $\mathbf{E}_\perp$ is implemented. In the original simulations (Figure 1a; e.g. Yeates et al. 2010), $\mathbf{E}_\perp$ is given by a surface flux transport model with imposed flows, whereas in the new simulations (Figure 1b), $\mathbf{E}_\perp$ is determined directly from a sequence of surface magnetic maps. For the single and multiple bipole simulations the hyperdiffusion coefficient is set to zero, whereas in the simulations using the ADAPT maps it is $1 \times 10^{11} \mathrm{km}^4/\mathrm{s}$.
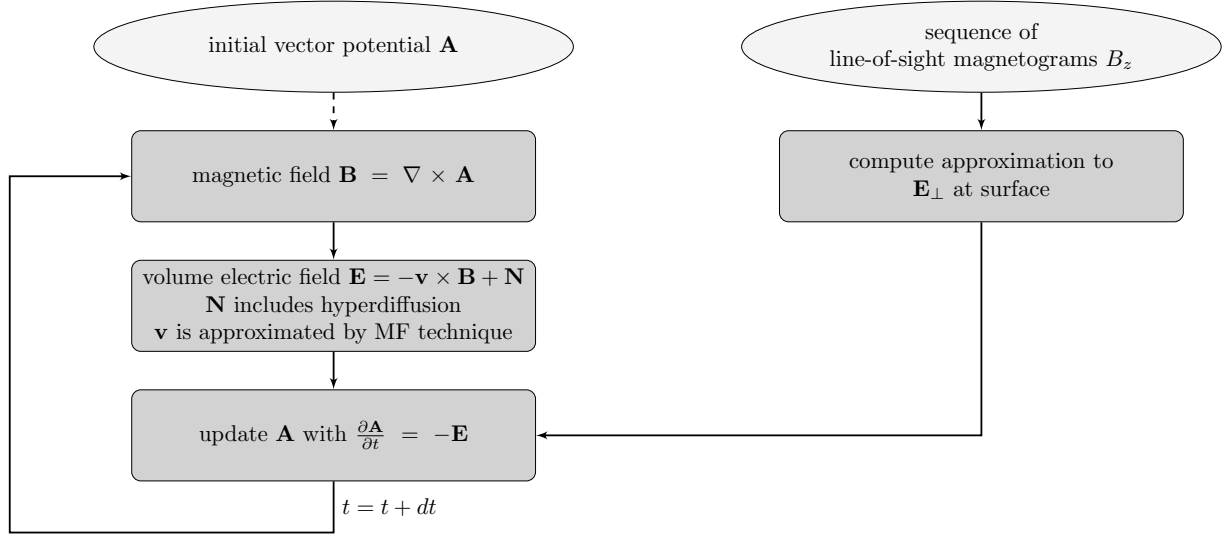
All of the simulations in this paper use a fixed, regular spherical grid $R_\odot \leq r \leq 2.5 R_\odot$, $8.3° \leq \theta \leq 171.7°$ (i.e., the poles are cut off), $0° \leq \phi \leq 360°$, with grid cells equally spaced in the stretched coordinates x, y, z (see Appendix A.1), with 28 cells in radius, 160 cells in latitude, and 192 cells in longitude. At latitudinal boundaries ($\theta = 8.3°$ and $\theta = 171.7°$), we impose $B_\theta = v_\theta = 0$. The inner boundary conditions (at $r = R_\odot$) are the main subject of this paper (see Sec. 4). At the outer boundary ($r = 2.5 R_\odot$), we follow our previous simulations and impose zero radial gradient in B_θ and B_ϕ, along with a radial outflow to ensure that $\mathbf{B}$ remains predominantly radial near this boundary, while allowing flux ropes to be ejected (cf. Mackay & van Ballegooijen 2006; Yeates et al. 2010).

3. INPUT DATA

In this paper, we consider three different sequences of $B_r(\theta, \phi, t)$ for the photospheric boundary conditions, with corresponding initial conditions for $\mathbf{B}(r, \theta, \phi, \mathbf{t} = \mathbf{0})$. Two sequences are taken from our own surface flux transport simulations, while the third is taken from the ADAPT model. From first to third, the test sequences have decreasing amounts of available information about

initial vector potential $\mathbf{A}$

insert bipoles into $\mathbf{A}$

magnetic field $\mathbf{B} \;=\; \nabla \times \mathbf{A}$

surface electric field $\mathbf{E}_\perp$
from flux transport model

volume electric field $\mathbf{E} = -\mathbf{v} \times \mathbf{B} + \mathbf{N}$
$\mathbf{N}$ includes hyperdiffusion
$\mathbf{v}$ is approximated by MF technique

update $\mathbf{A}$ with $\frac{\partial \mathbf{A}}{\partial t} \;=\; -\mathbf{E}$

$t = t + dt$

(a) The evolution of the magnetic field in the original MF simulation.

initial vector potential $\mathbf{A}$

sequence of
line-of-sight magnetograms B_z

magnetic field $\mathbf{B} \;=\; \nabla \times \mathbf{A}$

compute approximation to
$\mathbf{E}_\perp$ at surface

volume electric field $\mathbf{E} = -\mathbf{v} \times \mathbf{B} + \mathbf{N}$
$\mathbf{N}$ includes hyperdiffusion
$\mathbf{v}$ is approximated by MF technique

update $\mathbf{A}$ with $\frac{\partial \mathbf{A}}{\partial t} \;=\; -\mathbf{E}$

$t = t + dt$

(b) The evolution of the magnetic field in the MF simulation using magnetograms on the photospheric boundary to drive the simulation.

Fig. 1.— Simulation Flowcharts.

$\mathbf{E}_\perp$, in addition to the sequence of B_r itself. Using test cases where $\mathbf{E}_\perp$ is known allows us to validate our reconstructed $\mathbf{E}_\perp$, as well as to compare 3D output quantities such as photospheric flux, open flux, magnetic energy, or electric current. In principle, any data processed to give a 360° radial magnetic map of the Sun can be used as input to our method. However, we will see in Sec. 5.3 that the quality of the map (for example how new data is assimilated) has an impact on the outcome. As the method is not limited to larger spatial scales, future simulations (given sufficient computing resources) could model local regions of the Sun directly from observed magnetograms at their full resolution. An application of a similar technique to active regions observed by SOHO/MDI can be seen in Gibb et al. (2014).

3.1. Single-Bipole Simulation

For this sequence, a single bipolar magnetic region is evolved for over 1200 hours (50 days), under the influence of surface flux transport effects, but with no flux emergence during the simulation (cf. Mackay & van Ballegooijen 2001, 2005, 2006). Here the sequence of $B_r(\theta, \phi, t)$ maps is computed from the surface flux transport model, whose electric field $\mathbf{E}_\perp(\theta, \phi, t)$ is known completely and given by

$$\mathbf{E}_\perp = -\mathbf{v} \times (B_r \mathbf{e}_r) + D\nabla \times (B_r \mathbf{e}_r), \quad (2)$$

where $D = 500\,\mathrm{km}^2\,\mathrm{s}^{-1}$ is the supergranular diffusivity and $\mathbf{v}$ is a steady axisymmetric flow comprising a poleward meridional flow u_θ (due to Schüssler & Baumann 2006) along with differential rotation u_ϕ (Snodgrass 1983), expressed in the Carrington frame, given by

$$u_\theta = u_0 \frac{16}{110}\sin(2\lambda)\exp(\pi - 2|\lambda|), \quad (3)$$

$$u_\phi = \Omega(\phi)R_\odot\sin\theta, \quad (4)$$

$$\Omega = 0.18 - 2.3\cos^2\theta - 1.62\cos^4\theta\,\mathrm{deg\ day}^{-1},$$

with $\lambda = \pi/2 - \theta$ and u_0 a constant controlling the flow amplitude. The $B_r(\theta, \phi, t)$ map is saved once per hour, in order to test our reconstruction of $\mathbf{E}_\perp$.

The initial magnetic bipole takes the form given by Mackay & van Ballegooijen (2001), which also defines its initial 3D magnetic field for the MF simulations. This initial 3D magnetic field is not potential, but includes a non-zero twist in the centre

of the bipole. For this test, the bipole is embedded in a weak background magnetic field, computed by assuming a potential field with $B_r(R_\odot, \theta, \phi) = 0.01\cos^7\theta$.

3.2. Multiple-Bipole Simulation

The second sequence of $B_r(\theta, \phi, t)$ is taken from the same surface flux transport model as the single-bipole simulation. The main difference is that now multiple bipolar regions emerge during a continuous evolution over 1512 hours (63 days). This represents the photospheric driver used in the global MF simulations that have been carried out to date by Yeates et al. (2008); Yeates et al. (2010); Yeates & Mackay (2012); Yeates (2014). The simulation is initialized with a potential-field extrapolation from an observed synoptic magnetogram (corrected for differential rotation). The simulated time is 2012 September 11, 12:00 UT, to 2012 November 13, 12:00 UT.

In this case, $\mathbf{E}_\perp$ still follows the known evolution described by flux transport processes (2) between emergence events. However, the new bipoles emerge instantaneously (always at 12:00 on the corresponding day), following the method described by Yeates et al. (2008). The $B_r(\theta, \phi, t)$ sequence is therefore discontinuous in time, with each bipole emergence corresponding to an instantaneous impulse of $\mathbf{E}_\perp$ of infinite strength. We will show in Section 5.2 how our method of reconstructing $\mathbf{E}_\perp$ approximates this impulse with an electric field of finite strength and duration, depending on the chosen cadence between maps in the B_r sequence.

3.3. ADAPT Maps

Our third sequence of $B_r(\theta, \phi, t)$ is taken from the the global magnetic maps generated by the ADAPT model. ADAPT uses a photospheric flux transport model based on that of Worden & Harvey (2000), together with data assimilation techniques (in this case, ensemble least squares) from the Los Alamos National Laboratory (LANL) framework, in order to generate more realistic global photospheric magnetic field maps. The flux transport model includes differential rotation and meridional flow similar to the model used in Sections 3.1 and 3.2. However, instead of a simple diffusion model of supergranulation, it models the

small-scale clumping of magnetic flux on the solar surface through a combination of random attractors and random daily background flux emergence.

Magnetograms from the National Solar Observatory (NSO) Global Oscillation Network Group (GONG; Harvey et al. 1996) are used as the input data source to produce the ADAPT maps used in this work.. The ADAPT model assimilates new observations once per day from line-of-sight magnetograms, or, if no new observations are available (due to the weather), from the evolved model. Between the daily data assimilation steps, maps of $B_r(\theta, \phi, t)$ are output every two hours from the model, and it is these maps that we use as input. The sequence of maps used here runs from 2014 November 1, 00:00 UT to 2014 December 23, 22:00 UT (1270 hours). None of the maps we use corresponds exactly to the time of data assimilation.

While the data assimilation ensures that Earth-facing regions of the solar surface match more closely to observations, it does mean that the true $\mathbf{E}_\perp$ is not known for the ADAPT sequence. This is in contrast to the bipole simulations where it is known. As a result, it is important to begin by testing the electric field inversion on known cases of the bipole sequences, before applying it to the ADAPT sequence.

As only half of the Sun is visible from the Earth at one time, the far-side data in the ADAPT maps are outdated, using only previous observations and the flux transport model. The data for these regions are only updated as the regions appear again on the east limb, with the data assimilation technique taking into account the observational errors at the limb. This, however, creates a discontinuity in the data at the respective longitude, particularly when significant flux emergence or active-region evolution has taken place on the far side. This has some effect on the simulation, as we will see in Sec. 5.3.

Before computing $\mathbf{E}_\perp$, we rotate the ADAPT maps into the Carrington frame, interpolate them to match our computational grid (from an original resolution of 360×180) and remove any monopole component by a multiplicative flux correction. The ADAPT maps come as an ensemble of twelve realizations, which account for model parameter uncertainties in the supergranular flow. We arbitrarily picked one of this realizations for our runs in Sec. 5.3, although we have verified that the results are only slightly changed if a different realization is selected.

4. METHODS FOR ELECTRIC FIELD INVERSION

The basic problem is to determine $\mathbf{E}_\perp$ from B_r, where the two quantities are related through the radial component of Faraday's law:

$$\frac{\partial B_r}{\partial t} = -\mathbf{e}_r \cdot \nabla \times \mathbf{E}_\perp. \qquad (5)$$

It is convenient to make a Helmholtz decomposition of $\mathbf{E}_\perp$ (e.g., Amari et al. 2003; Fisher et al. 2010) and express it as

$$\mathbf{E}_\perp = -\nabla \times \left(\frac{\partial \Phi}{\partial t} \mathbf{e}_r \right) - \nabla_\perp \frac{\partial \psi}{\partial t}, \qquad (6)$$

where the time derivatives are included for later convenience. As we will show below, the potential $\Phi(\theta, \phi, t)$ may be determined from a sequence of B_r maps using Equation (5) (see also Fisher et al. 2010; Yang et al. 2012; Cheung & DeRosa 2012). For this reason, we call the first part of the decomposition the "inductive component".

In contrast, the potential $\psi(\theta, \phi, t)$ is impossible to determine from B_r using Equation (5), since the horizontal gradient vanishes under the operation $\mathbf{e}_r \cdot \nabla \times$. We call this the "non-inductive" component. This freedom means that the total electric field $\mathbf{E}_\perp$ is not uniquely-determined by B_r alone. The simplest practical solution is to ignore the non-inductive component (i.e., set $\psi = 0$), as in the works of Mackay et al. (2011), Yang et al. (2012) and Gibb et al. (2014). However, we will show that this component is non-negligible in our bipole simulations, leading to significant differences in the coronal magnetic field. We will therefore propose, in Section 4.2, a practical first-order approximation to this component for global simulations.

4.1. Purely Inductive Solution

For a given sequence $B_r(\theta, \phi, t)$, the inductive component $-\nabla \times (\partial \Phi / \partial t \, \mathbf{e}_r)$ is uniquely determined for suitable boundary conditions. To appreciate the solution uniqueness, substitute Equation (6) into Faraday's law (5) to obtain the two-

dimensional Poisson equation

$$\nabla_\perp^2 \frac{\partial \Phi}{\partial t} = -\frac{\partial B_r}{\partial t}. \tag{7}$$

In practice, we follow Mackay et al. (2011) in the equivalent method of first solving the Poisson equation

$$\nabla_\perp^2 \Phi = -B_r, \tag{8}$$

then taking the time derivative. On the full sphere, this equation would have a unique solution for Φ. However, our simulation domain omits the poles, so it is necessary to impose boundary conditions on the θ-boundaries. As a physically reasonable choice we take Neumann boundary conditions $\partial\Phi/\partial\theta = 0$, so that $E_\phi = 0$ on these boundaries, consistent with global magnetic flux conservation. To solve the Poisson equation, we have implemented a spherical multigrid solver (see Appendix A.2).

The purely-inductive approximation

$$\mathbf{E}_\perp = -\nabla \times \left(\frac{\partial \Phi}{\partial t} \mathbf{e}_r \right) \tag{9}$$

is, computationally speaking, the simplest electric field consistent with a given B_r sequence. To illustrate that in the global simulations this term alone is not satisfactory, Fig. 2 shows a snapshot of the purely-inductive $\mathbf{E}_\perp$ components E_θ, E_ϕ derived from the multiple-bipole sequence, alongside the true electric field components (from the flux transport simulations). It can be clearly seen, in particular at high latitudes, that the inductive-only version neglects to include the East-West structures (most obviously for E_θ) which are a consequence of differential rotation. It is not surprising that the inductive component misses this as at higher latitudes the field becomes more axisymmetric. As a consequence differential rotation has the effect of acting along contours of the same value of B_r. Thus when the time derivative of Eqn. 8 is taken no change is found. The next section describes our approach to improve the approximation to $\mathbf{E}_\perp$; further comparisons will be given in Section 5.

4.2. Non-inductive Component

Fisher et al. (2012) and Kazachenko et al. (2014) use additional observations (e.g., Doppler velocities) and assumptions (such as ideal Ohm's law) in order to estimate the non-inductive component $-\nabla_\perp \partial\psi/\partial t$ in individual active regions. These additional measurements, however, are not routinely available for the full solar surface including the far side.

Here, we propose an alternative way to approximate the non-inductive component, using only routinely available global line-of-sight magnetograms and knowledge of large-scale differential rotation. Our approach is motivated by the observation that, for the multiple-bipole sequence, the purely-inductive approximation works well for a sequence where differential rotation is turned off. This is shown in Fig. 3, where both E_θ and E_ϕ show much better agreement than in the original Fig. 2.

Since we know the differential rotation velocity $\mathbf{v} = v_\phi(\theta)\,\mathbf{e}_\phi$ that produced the multiple-bipole sequence, we can include the corresponding non-inductive component from the ideal Ohm's law $\mathbf{E}_\perp = -\mathbf{v}\times(B_r\mathbf{e}_r)$. Taking the divergence removes the inductive component, leaving a new Poisson equation

$$\nabla_\perp^2 \frac{\partial \psi}{\partial t} = \nabla \cdot \left(v_\phi B_r\, \mathbf{e}_\theta \right), \tag{10}$$

which we solve to give an approximation to $\partial\psi/\partial t$. For consistency with the the inductive part, we have to impose homogenous Dirichlet boundary conditions (i.e., $\psi = 0$) on the θ boundary. Since in global simulations differential rotation is the dominant large-scale flux-transport effect with a time-scale of $1/4$ year, we expect that this will be the dominant contribution to the non-inductive electric field, at least away from times when new bipoles emerge. The correction may also be applied to the ADAPT sequence, which we show to produce reasonable results, although we will see that the purely-inductive solution actually works rather well in that case.

Fig. 4 shows that the reconstructed electric field components, which include the non-inductive component, are in better agreement with the original multiple-bipole sequence. In the following section, Sec. 5, we discuss the effect of the reconstructed non-inductive component in more detail for the for the simulations with different input sequences.

(a) E_ϕ original multiple bipole simulation.

(b) E_ϕ inductive-only reconstruction.

(c) E_θ original multiple bipole simulation.
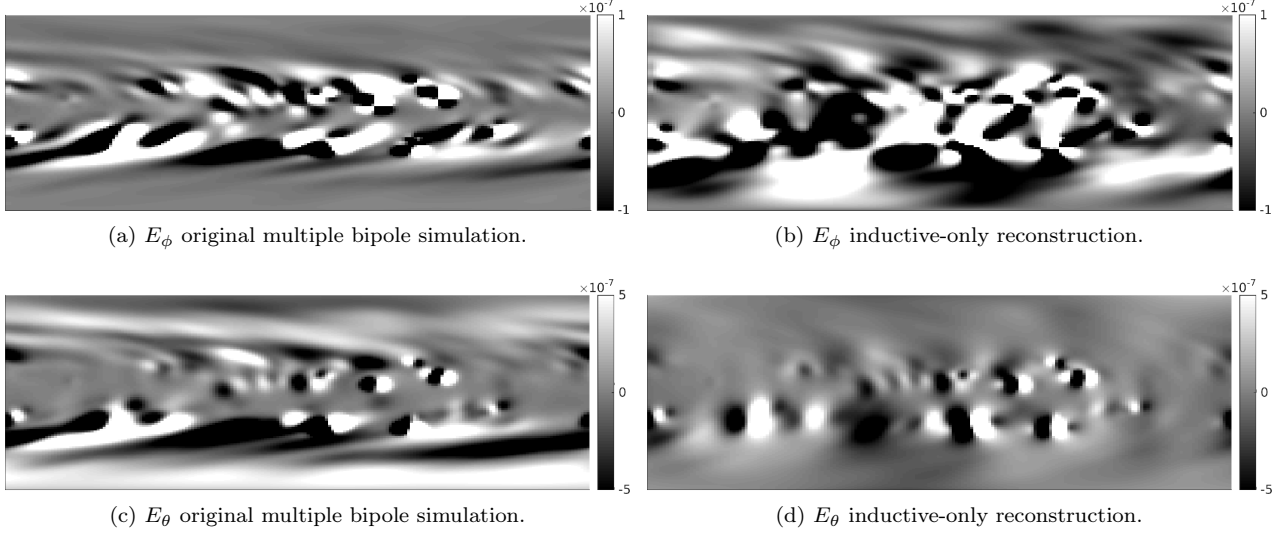
(d) E_θ inductive-only reconstruction.

Fig. 2.— Electric field components E_θ and E_ϕ 984 hours into the original and inductive-only multiple bipole simulation. The original simulation and therefore also the input maps for the data-driven simulation include differential rotation.
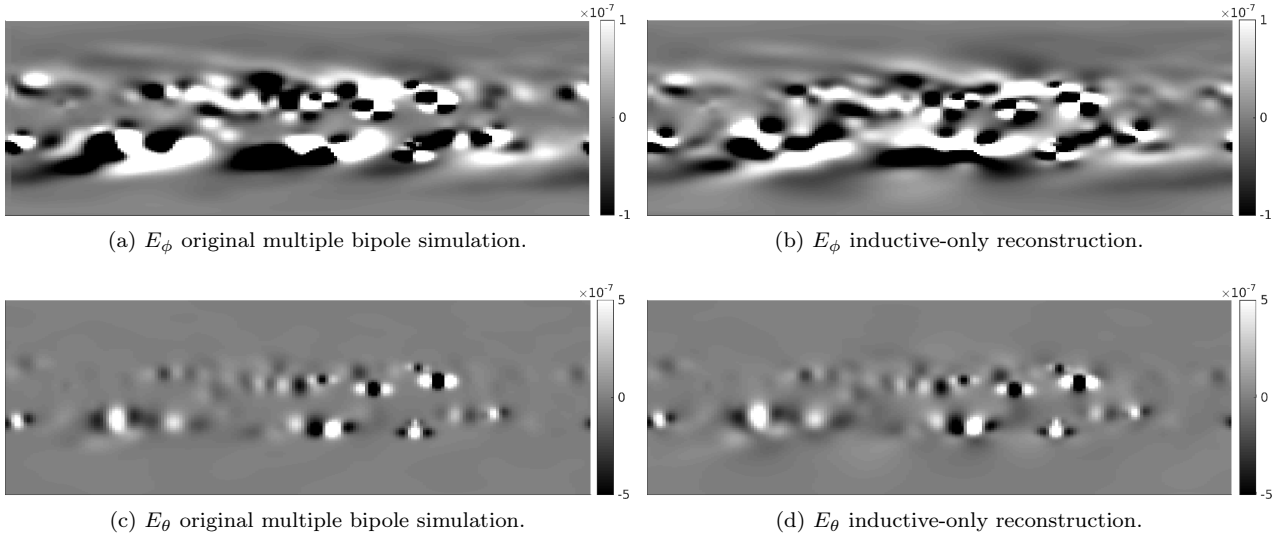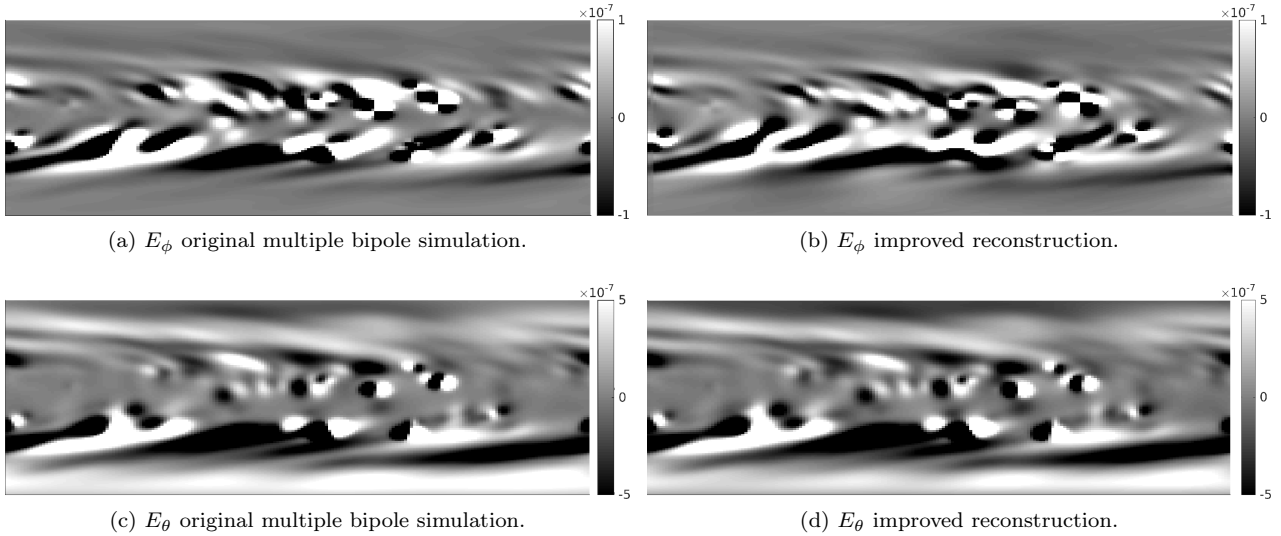

(a) E_ϕ original multiple bipole simulation.

(b) E_ϕ inductive-only reconstruction.

(c) E_θ original multiple bipole simulation.

(d) E_θ inductive-only reconstruction.

Fig. 3.— Electric field components E_θ and E_ϕ 984 hours into the original and inductive-only multiple bipole simulation. Here, the original simulation and therefore also the input maps for the data-driven simulation do not include differential rotation.

(a) E_ϕ original multiple bipole simulation.

(b) E_ϕ improved reconstruction.

(c) E_θ original multiple bipole simulation.

(d) E_θ improved reconstruction.

Fig. 4.— Electric field components E_θ and E_ϕ 984 hours into the original multiple bipole simulation and the improved-reconstruction multiple bipole simulation (i.e., including the non-inductive part). The original simulation and therefore also the input maps for the data-driven simulation include differential rotation.

5.   RESULTS

5.1.   Single-Bipole Sequence

The comparisons in Figures 2, 3, and 4 suggest that including a non-inductive component in the reconstruction of $\mathbf{E}_\perp$ can improve the match to the original flux-transport $\mathbf{E}_\perp$, at least away from times of flux emergence. To quantify the effect more carefully, we begin by examining 3D simulation results for the simplest case of a single-bipole time sequence.

Figure 5 shows four diagnostic quantities for the non-potential simulations. The different curves show a simulation driven by the original $\mathbf{E}_\perp$ (green), one driven by the purely-inductive $\mathbf{E}_\perp$ (red), and one driven by the combined ("improved") $\mathbf{E}_\perp$ (i.e., including our approximation of the non-inductive component, blue line). While the photospheric flux is the same in all cases (since all three $\mathbf{E}_\perp$ produce the same B_r), the benefit of the combined reconstruction becomes clear from the three coronal diagnostics. The most significant feature of this particular MF simulation is the gradual formation and strengthening of a flux rope above the bipole centre (cf. Mackay & van Ballegooijen (2006); Mackay (2006) for a similar case study), followed by its sudden eruption (after

about 670 hours in the original simulation). The rise and ejection of this flux rope is most obviously seen in the open flux. Whilst both reconstructions lead to an eruption, only the combined reconstruction reproduces the original simulation timing. The timing of the ejection is delayed by almost 500 hours in the purely-inductive simulation. The combined solution follows the original simulation closely, with only a short delay in the eruption. It is also clear that for the magnetic energy and electric current the combined simulation produces a much more realistic reproduction of the original simulation. This indicates that differential rotation which is included through the non-inductive term plays a key role in the evolution of the coronal field.

Fig. 6 exhibits model snapshots of the magnetic field lines, traced from identical starting points, before and after the original flux rope eruption. The bipole can be seen in black and white on the grey sphere. The three cases are compared in Fig. 6, for example, after 240 hours (shown in the first row), the shape of the field lines is still quite similar in all three cases, however, by 600 hours (middle row) the original (green) and improved reconstruction (blue) plots show a strongly sheared field over the polarity inversion line (PIL). This
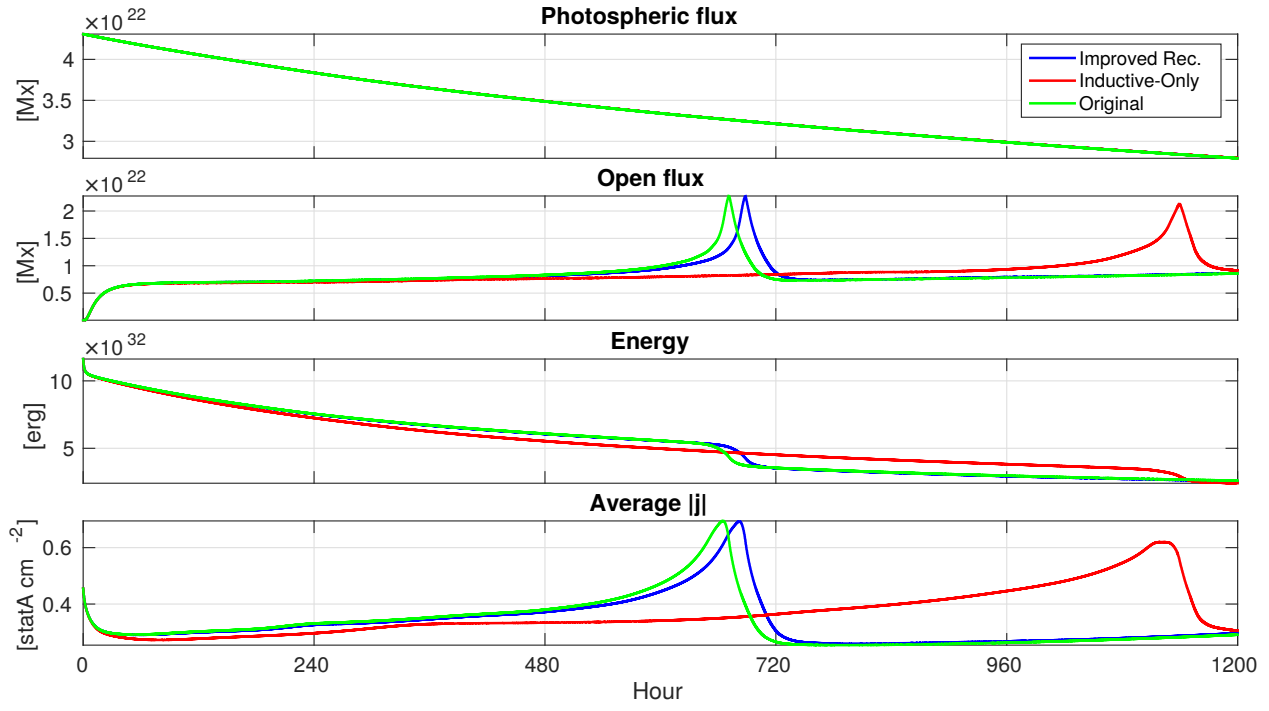
Fig. 5.— Integrated quantities in the single-bipole simulations. The top panel shows the total unsigned magnetic flux through the photosphere, the second panel represents the total unsigned open magnetic flux (i.e., through the outer boundary), the third panel depicts the total magnetic energy, and the fourth panel features the averaged electric current $|\mathbf{j}|$ in the volume.
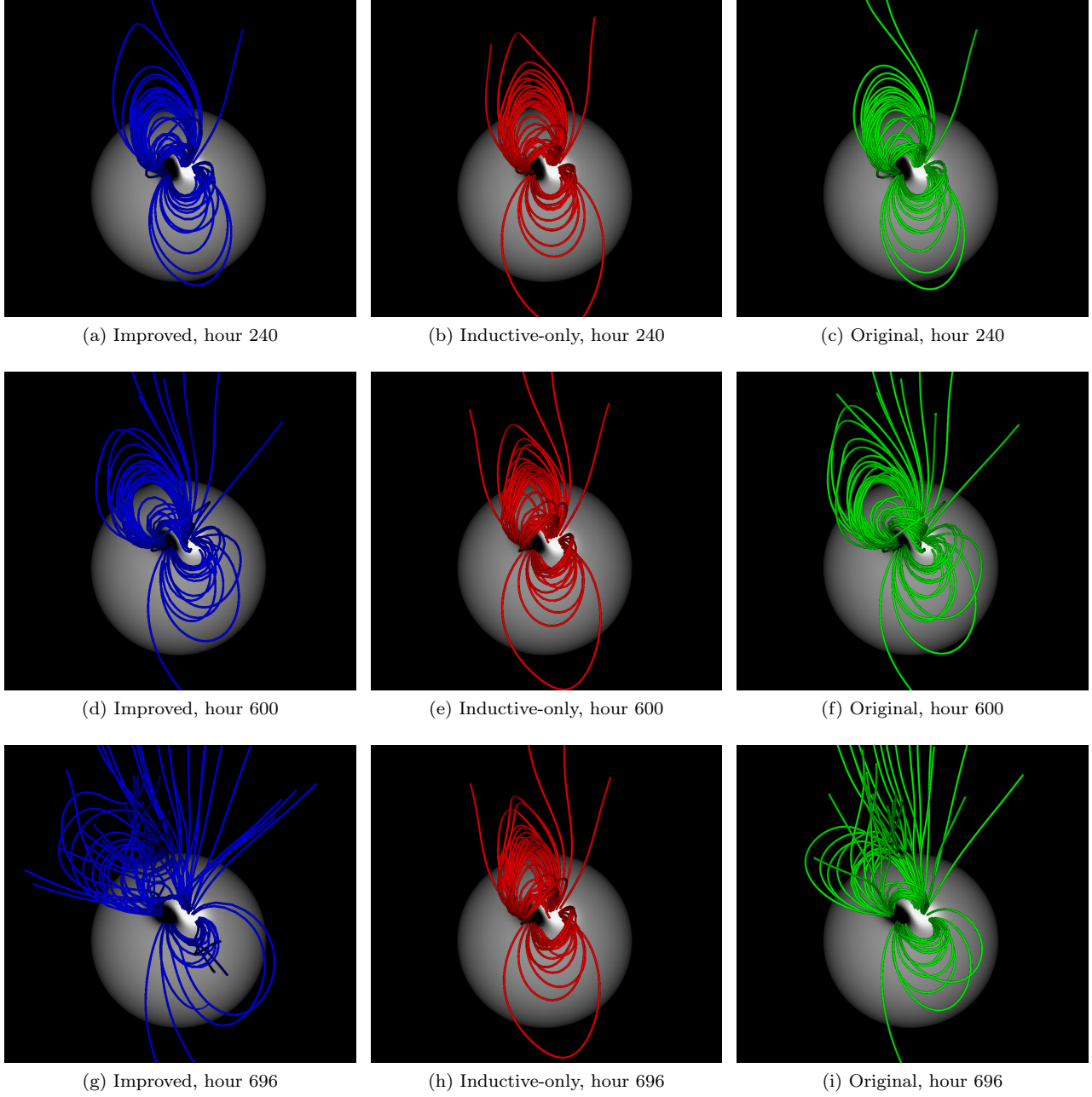
(a) Improved, hour 240   (b) Inductive-only, hour 240   (c) Original, hour 240

(d) Improved, hour 600   (e) Inductive-only, hour 600   (f) Original, hour 600

(g) Improved, hour 696   (h) Inductive-only, hour 696   (i) Original, hour 696

Fig. 6.— Selected magnetic field lines illustrate the single bipole simulation at different times during the evolution. The original simulation (green) and the improved-reconstruction simulation (blue) quickly build up sheared field (first two rows) above the polarity inversion line of the bipole and then erupt. In the last row, the original field lines have almost settled down after the eruption, while the improved-reconstruction field lines have just started to settle. The inductive-only simulation (red) builds up the sheared field much more slowly, resulting in a much later eruption (not shown in this figure).

11

strongly sheared field is not present for the case for the inductive-only plot (red). In the bottom row (hour 696), the original field lines have already almost settled down again after the eruption and the combined reconstruction field lines have just erupted, whereas the inductive-only field lines are still in the process of building up a sheared field. Overall the structure and shape of the blue and green field lines are very similar.

To quantify the amount of sheared field built up above the PIL, Yeates & Mackay (2012) defined a measure called "skew". This is the sine of the angle between the horizontal field $\mathbf{B}_\perp$ at a certain height $r > R_\odot$ and the direction ∇B_r (normal to the PIL) in the photosphere, i.e.:

$$\sin\gamma = \frac{\mathbf{e}_r \cdot \nabla B_r \times \mathbf{B}_\perp}{|B_r||\mathbf{B}_\perp|}. \tag{11}$$

A magnitude of $|\sin\gamma| = 1$ indicates that the field at height r is directed along the PIL, while $\sin\gamma = 0$ indicates that the field is perpendicular to the PIL. Here we use $\sin\gamma$ to compare the amount of horizontal magnetic field built up in the corona by the different reconstructions of $\mathbf{E}_\perp$. Figure 7a shows the maximum skew (along the length of the PIL) at a height $r = 0.3448R_\odot$, for the three cases. The skew increases until the flux rope erupts in each case, and then declines rapidly. Again, the simulation driven by the combined reconstruction matches the original simulation closely in this measure, while the build-up of skew is significantly slower in the purely-inductive case. Clearly the non-inductive electric field from differential rotation makes an important contribution here.

An alternative comparison between the inductive and combined reconstructions is given by Fig. 7b, which shows the correlation between B_θ (B_ϕ gives similar results) between each simulation and the original (averaged over r). The correlation is almost perfect for the improved reconstruction, except for a dip around the time of the flux rope eruption. This corresponds to the slight delay in the eruption compared to the original simulation, likely due to the omitted contribution of supergranular diffusion to the non-inductive electric field. For the purely-inductive simulation, the correlation is significantly worse at all times.
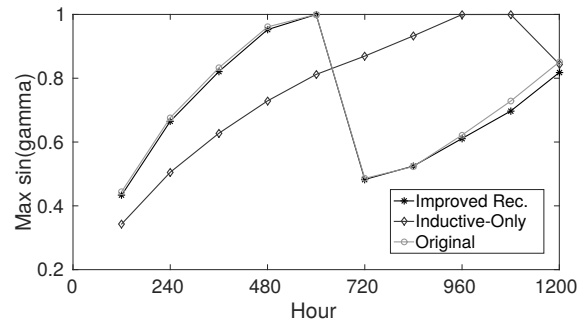
(a) Maximal skew at height $r = 0.3448R_\odot$ (z=4) over time.
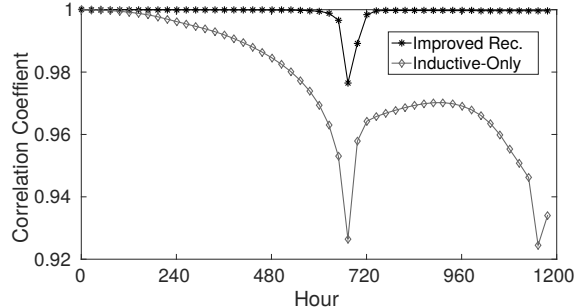
(b) Correlation of simulated B_θ (averaged in r) between each reconstruction and the original simulation.

Fig. 7.— Comparison of different $\mathbf{E}_\perp$ reconstructions for the single-bipole sequence.
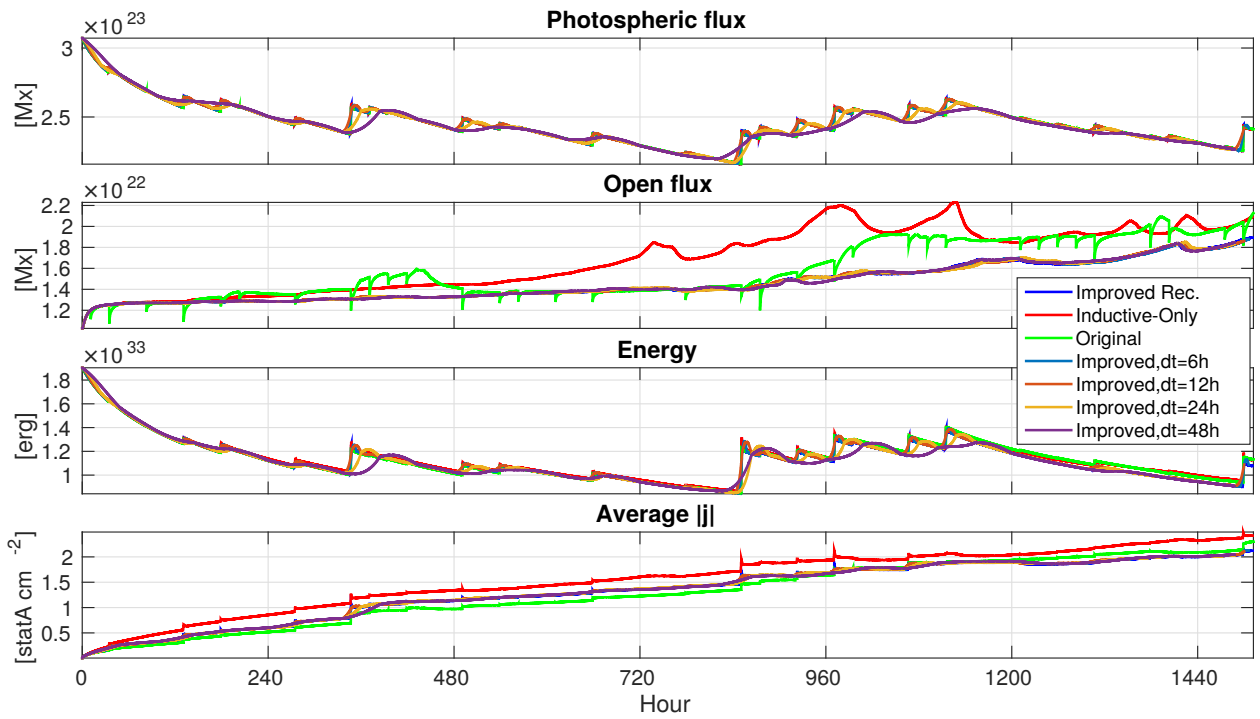
Fig. 8.— The same quantities as in Fig. 5 but for the multiple-bipole simulations, including the purely-inductive reconstruction and a sequence of combined reconstructions with different time intervals dt between input maps. The first three curves used $dt = 1h$.

13

5.2. Multiple-bipole sequence

We have already seen in Figures 2 and 4 how including the non-inductive component improves the agreement of our simulated electric field with the original field from the multiple bipole simulation. Fig. 8 shows how other simulated quantities, including magnetic flux, magnetic energy and electric current, differ when we omit or include the non-inductive component in the multiple bipole simulation. For the original simulation (green line) one can see the jumps in energy and photospheric flux, and the corresponding drops in the open flux, when new bipoles are inserted into the simulation domain. These drops are not visible in the two reconstructed versions, as they are due to the idealised bipole insertion procedure of the original simulation and vanish when we interpolate the electric field between the times when new B_r maps are imposed. The photospheric flux matches closely, as it is imposed each time a new map is incorporated for both reconstruction cases. The total electric current and the magnetic energy match quite closely for both cases, although the inductive-only simulation leads to a slightly higher average current. The difference in open flux becomes larger over time, with more open flux and a bigger difference to the original simulation in the inductive-only case.
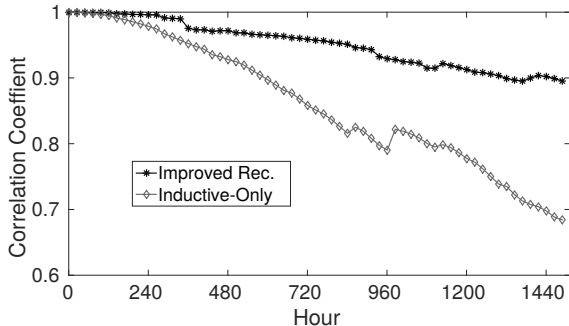

Fig. 9.— Correlation coefficient (averaged over r) of B_θ in the improved-reconstruction multiple bipole simulation and the inductive-only reconstruction multiple bipole simulation, respectively, with the original simulation.

The plots in Fig. 9 show the progression of the correlation coefficient values with time between B_θ of the two data-driven runs, and that of the original simulation. The correlation is initially very

good, but decreases with time. It is clear that the improved reconstruction produces much better results with its correlation staying above 0.9 over the entire simulation. In contrast by the end the inductive only simulation has a correlation of 0.7. The decrease of correlation over time in both cases is due to an accumulation and propagation over time of small deviations, owing to the "memory" for previous interactions in the MF model. The correlation values in Fig. 9 were averaged over depth r. If we instead look at the correlation over r, we observe that there is also a drop when we move higher up into the corona. This is due to the fact that, while the field is line-tied near the photosphere where the boundary conditions are imposed, the field has more freedom further away from the fixed layer.

In addition, Fig. 8 demonstrates how the diagnostic quantities discussed above change for the improved reconstruction case when we vary the cadence between the input maps, i.e., the frequency of imposing new photospheric boundary conditions. The curves are very close and always coincide at the input times. In between, the interpolation of the electric field produces a smooth curve. The effect of newly inserted bipoles is missed when the time step between new boundary conditions $dt > 24h$ (the cadence at which new bipoles emerged in the original simulation). This highlights that in any future application of this technique to the solar corona it is very important that the cadence for the input of maps is less than the cadence of introducing new emergences into the observed maps. Only through doing this will the full dynamics of the coronal field be captured.

Increasing the time step dt (and thus decreasing the cadence) reduces the computational costs of the simulation slightly, as each time we impose a new electric field we have to solve two Poisson equations. This takes a few seconds on an average workstation using our multigrid Poisson solver (see Sec. A), but that adds up over the whole simulation run. However, one does not gain anything in the time stepping process, which dominates the computational load. Note that the results in Sec. 5.3 indicate that the ADAPT maps are more sensitive to a change in dt.

We tested two alternative computational methods for imposing the photospheric boundary conditions: (i) interpolating the input maps B_r and

calculating a new electric field for each time step; and (ii) using the same electric field for the whole hour until a new electric field is imposed. (Our original method was to interpolating the electric field between input maps.) The first alternate method increases the computational workload hugely, whereas for the second method the gain in computational time is minimal. We did not find significant differences or improvements in the output with these methods.

5.3. ADAPT Simulation

Fig. 10 shows the same quantities for the ADAPT simulation as seen previously for the single and multiple bipole cases. In the photospheric flux and (less distinctly) in the magnetic energy, one can see when new data are assimilated in the ADAPT data set once per day. Overall, the two curves of improved and inductive-only cases are much closer than in the runs with the single and multiple bipole sequences. This is due to the presence of small-scale features in the ADAPT maps (see Fig. 11), compared to the smooth average B_r in the previous flux transport model. The motion of these small-scale features allows the inductive electric field to better capture the advection of footpoints by differential rotation than in the bipole simulations, since the field at this location is no longer axisymmetric. In the bipole simulations, on the other hand, we have more large-scale features along the direction of the differential rotation (as in Fig. 4). With a more or less constant B_r along this flow direction, the motion is missed by the inductive component of the electric field. The higher values for the photospheric flux and the total current for the run with the ADAPT sequence are also due to the inclusion of small scale features.

Although at first sight it might seem that the purely-inductive reconstruction is sufficient for this sequence of B_r maps, there are still times where the two simulations differ. This can be most easily seen in the open flux displayed in Fig. 10, where around hour 1000 more smooth large scale features occur in the ADAPT maps. Therefore the non-inductive component is still important to capture the evolution of these features. It will be interesting to consider in future work how the inductive-only and the combined electric fields influence simulations over larger time-scales.

One feature that catches the eye in the ADAPT tests is the large drop in energy around hour 352 in the simulation. Fig. 11 demonstrates what happens in the simulation at that time: a large active region southern hemisphere (AR12209, which was AR12192 in the previous rotation) changes its structure while it is on the far-side of the sun. This change is recognised in the simulation when this region rotates into view. The large sudden change in the magnetic field results in a large electric field, due to Eq. (6), which in turn influences the magnetic field, leading to a rapid rearrangement of magnetic field lines (discussed below). As we solve Poisson equations for the electric field, i.e. elliptic equations, the effect of this change is felt further into the domain, and creates the halos that we can see in the middle column of Fig. 11 (note the change of scale for the electric field components). After a short time, this defect is corrected by the simulation as can be seen in the right hand column of Fig. 11. Similar halo effects can be seen when new bipoles are inserted in the multiple bipole simulation, and have been observed by Kazachenko, Fisher & Welsch (2015, private communication). We are currently testing methods to remove the halos or at least reduce them.

As shown in Fig. 12, during the assimilation of the new region the free energy in the simulation increases. This happens just after the "big drop", when the potential field energy drops due to the drop in the photospheric flux, and is related to disconnection happening in the magnetic field, as described in the next paragraph. Afterwards, it decays gradually back to a fairly constant value, but at a slightly higher level then before. This might be due to the assimilation in ADAPT and the corresponding electric field we chose. Future work might show to what extent the halo causes additional free energy outside the active region.

Looking at the magnetic field lines, we can observe that a large flux rope eruption takes place in our simulation shortly after AR12209 rotates into view (see Fig. 13), as was indicated by the peak in the open flux in Fig. 10. In the MF model, this eruption was inevitable since the photospheric flux content of the region decreased substantially on re-assimilation, leaving disconnected magnetic field lines in the corona. Thus while an eruption takes place it is due to the rapid, near instantaneous change in the surface field due to the as-
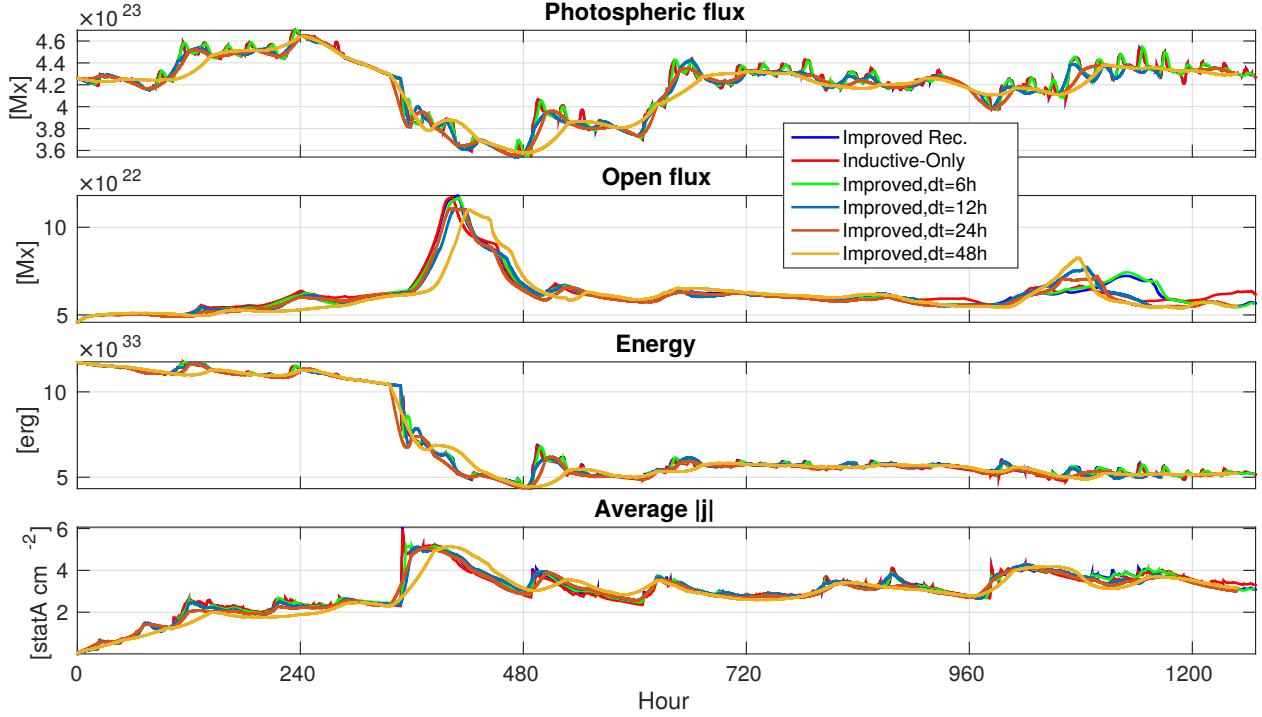
Fig. 10.— The same quantities as in Fig. 8 but for the ADAPT-driven simulation. Runs with varying time dt between input maps all use the improved reconstruction of $\mathbf{E}_\perp$. The first two curves used $dt = 2h$

similation technique. It is not as a consequence of the gradual process of building stress up in the coronal magnetic field by observed large-scale processes, as we have described before (Mackay & van Ballegooijen 2006).

One rotation later, around hour 1012, the same active region reappears as AR12237. A bit later, another hump in the open flux is visible, associated with another flux rope eruption. This later eruption is mainly due to a number of smaller bipoles which appear. Inspecting observational data for AR12192/12209 we find that in fact no eruptions took place at those times (as was to be expected). Instead, this region is known to have produced many, sometimes large, flares but only one associated CME during the previous rotation as AR12192 on the Earth-side, which is quite unusual (cf. Sun et al. 2015; Thalmann et al. 2015). Since only near-side data were assimilated, we did not find evidence for or against a CME when the region was on the far-side. As the flux rope eruptions in our simulation are associated with sudden rearrangement of the magnetic field lines due

to newly assimilated data, a smoother transition for structural changes which appear at the far-side might well change the nature or timing of associated eruptions in the simulation.

In comparison to Fig. 8, the variation of the time step size in Fig. 10 for the improved-reconstruction ADAPT simulation seems to have a larger impact, especially on the open flux. The smoothing of the (unphysical) peaks in the photospheric flux at the data assimilation times for larger dt may actually be beneficial. However, too large a value for dt may lead to actual physical effects being missed, if the photospheric maps are less smooth. Up to $dt = 6h$, the features of the curves still match each other pretty well, with just some smoothing added. However for the two open flux peaks (around hour 352 and after hour 1000) the open flux curves for larger dt are qualitatively different (in fact, $dt = 8h$, which is not shown here, matches the $dt = 2h$ curve also quite well until hour 1000, after which it becomes different).
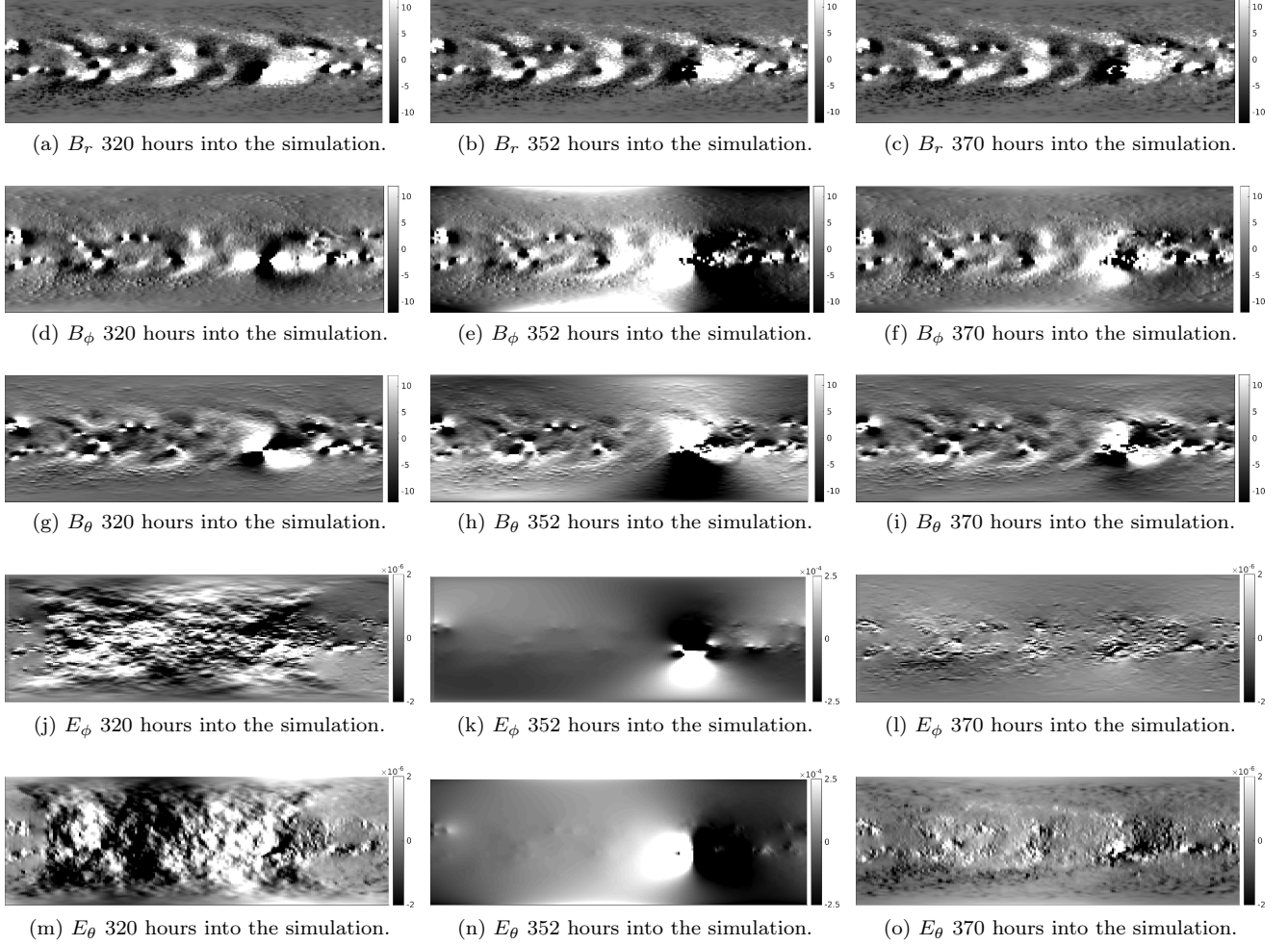
In Fig. 14 and 15 we show the current-helicity

16

(a) B_r 320 hours into the simulation.

(b) B_r 352 hours into the simulation.

(c) B_r 370 hours into the simulation.

(d) B_ϕ 320 hours into the simulation.

(e) B_ϕ 352 hours into the simulation.

(f) B_ϕ 370 hours into the simulation.

(g) B_θ 320 hours into the simulation.

(h) B_θ 352 hours into the simulation.

(i) B_θ 370 hours into the simulation.

(j) E_ϕ 320 hours into the simulation.

(k) E_ϕ 352 hours into the simulation.

(l) E_ϕ 370 hours into the simulation.

(m) E_θ 320 hours into the simulation.

(n) E_θ 352 hours into the simulation.

(o) E_θ 370 hours into the simulation.

Fig. 11.— The magnetic and electric fields during the big energy drop (assimilation of AR12209, which is the large active region in the bottom right quadrant of each field map, clearly visible in the top row) in the combined-reconstruction ADAPT simulation. Note the different scale for the electric field in the middle column.

density

$$\alpha = \frac{\mathbf{B} \cdot \mathbf{j}}{B^2} = \frac{\mathbf{B} \cdot (\nabla \times \mathbf{B})}{B^2}. \qquad (12)$$

Since the coronal magnetic field is close to force-free in the MF model, this quantity essentially illustrates the locations of electric current and free energy. We only show results for $dt \leq 24h$. The two chosen times are: (i) during the large flux rope eruption in the simulation following the appearance of AR12209, and (ii) just before it comes around again as AR12237. Interestingly, at this second time (hour 962), when all the lines in Fig. 8 match closely, the differences in α are quite large at some locations: in particular between $dt = 2$ and $dt = 6$, at around latitude 50°. For hour 386, on the other hand, α is rather similar for all the shown dt cases, despite the rather unpredictable behaviour of the field lines during the eruption. A more quantitative difference in the value of α can be seen in Fig. 15 where for the two cases shown in Fig. 14 the value of α averaged in longitude is shown as a function of latitude. Here the main difference at $\theta = 50°$ for hour 962 (Fig. 15b) is clear, where as the time step varies from 2 hours to 24 hours the value of α at this location changes significantly from positive to negative. In contrast, for hour 386 (Fig. 15a) the sign of α at a given latitude is the same no matter what cadence is used.

In the light of the discussion from Sec. 5.2 concerning the limited gain in computational time, the main issue about the choice of dt remains the availability of the B_r maps, which are mostly available at intervals of 24 hours. We should therefore keep in mind that this has a non-negligible influence on the simulation. One consequence of this is that in the future, wherever possible, a variety of cadences should be used along with ensemble averaging.

We mentioned already in Sec. 3.3 that the ADAPT data consist of an ensemble of twelve different realizations from which we deliberately picked realization 1 for our simulation. In Fig. 16 the same diagnostic quantities considered before are compared for the members of the ensemble. The curves match very closely, except from the open flux, which is, as we have seen before, the most sensitive quantity. Future longer simulation runs might show whether the choice of the realiza-
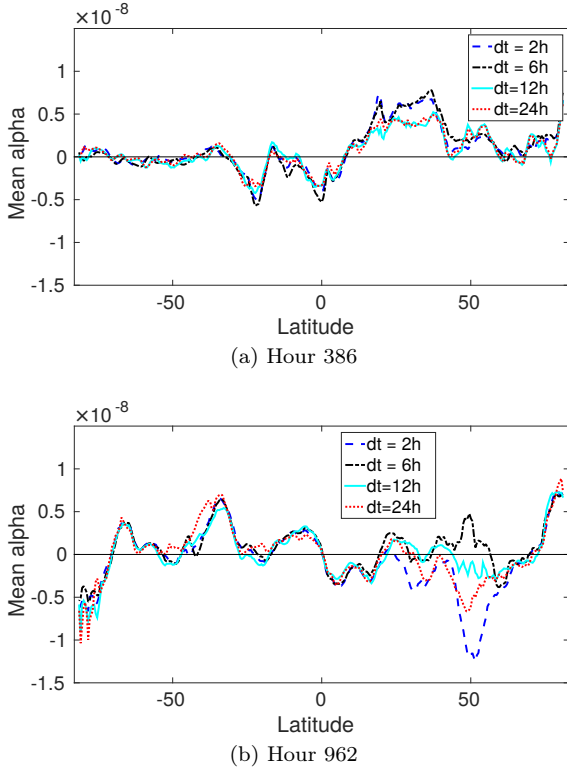

(a) Hour 386

(b) Hour 962

Fig. 15.— Mean α (i.e., current-helicity density α averaged over longitude) at height $r = 1.03327$ for different values of dt and at the same two times as in Fig. 14.

tion has a long-term significant influence on the simulation output.

6. CONCLUSION

We have demonstrated how a global non-potential coronal magnetic field simulation, using the magneto-frictional method, can be successfully driven by a time sequence of radial magnetic-field maps on the photosphere. Two possible solutions for the electric field reconstruction have been considered: a purely-inductive solution and one including a non-inductive correction. The second solution was motivated by tests with our existing flux-transport model, where it lead to a substantial improvement in reconstruction of the (known) electric field. The correction accounts for the non-inductive electric field caused by the large-scale differential rotation. We have also applied both electric fields to a sequence of maps from the ADAPT model, where the true electric field is not known (due to the assimilation of observed data). In this case, we find that correcting for the non-inductive contribution of differential rotation is less important, although it does have some effect later in the simulation.

Through varying parameters for the reconstruction of the photospheric electric field in the simulation, we found that the time step between the input maps has an effect that can become important at some points. For a time step of up to $dt = 6h$, we found the results to be reasonably close to the $dt = 2h$ simulation, but for larger dt differences such as earlier flux rope eruptions start to appear. In between the data input times it is sufficient to just interpolate the resulting electric field linearly.

There remain some limitations to our approach, which we are currently working on. For example, large and sudden changes in the photospheric field—for example when a new bipole appears or an active region that has changed its structure on the far-side is assimilated—lead to a large short-term increase of the electric field. This in turn can have a significant effect on the evolution of the coronal field such as the initiation of an eruption. Owing to the nature of our reconstruction, this change is felt outside the direct region of change in the photospheric magnetic map, potentially influencing the larger-scale free energy and open flux.

It will therefore be desirable, in future, to find an approach to electric field reconstruction (i.e., a choice of non-inductive component) that minimises these so-called halos. Alternatively, improved treatment of the assimilation discontinuity when constructing the ADAPT maps themselves may lead to improved simulation results for this data set. Recent work by Arge et al. (2013) describes how additional helioseismic far-side detection techniques can be used in order to detect new emerging large active regions on the far-side of the Sun and to assimilate these before they arrive at the east limb. Hickmann et al. (2015) describe further improvements of the ADAPT model, in particular by using local ensemble transform Kalman filtering instead of ensemble least squares. Using this improved data when it becomes available might reduce the effect of the unrealistic sudden changes in the photospheric field.

We have observed two different processes that can lead to a flux rope ejection: (i) a slow gradual build up of stress in the magnetic field, as described by Mackay & van Ballegooijen (2006) and (ii) rapid changes in the electric field, which are, in our case, partly due to the data assimilation technique in the ADAPT maps.

A further contribution to the non-inductive electric field that we have not yet included is that of additional magnetic helicity injection. This may arise either from the large-scale twisted fields in newly-emerging active regions (Yeates et al. 2007, 2008), or from the cumulative effect of small-scale vortical motions in the photosphere (Antiochos 2013; Mackay et al. 2014; Knizhnik et al. 2015). Both forms of helicity injection have been shown to influence the amount and distribution of free magnetic energy in the corona, however, neither form is fully accounted for in global radial-field maps. Even the inductive part of this contribution (due to the horizontal advection of B_r, for example) may be missed in current maps, because the growth of a particular active region may not be followed while it is on the far side of the Sun.

Nevertheless, we have demonstrated that magneto-frictional models of the corona may be successfully driven from sequences of photospheric magnetic maps. Our approximation to the non-inductive electric field due to differential rotation may also be useful in MHD simulations. This new technique may in the future be applied for space

weather models that use a combination of observations and theoretical modelling to simulate the variation of the Sun's open flux and flux rope ejections.
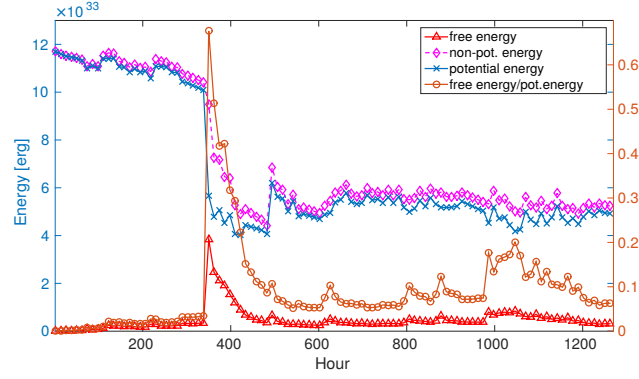
Fig. 12.— Evolution of the potential energy, non-potential energy, free energy and relative energy (free/potential energy, note the different y-axis) in the improved-reconstruction ADAPT simulation.

(a) Hour 340

(b) Hour 352
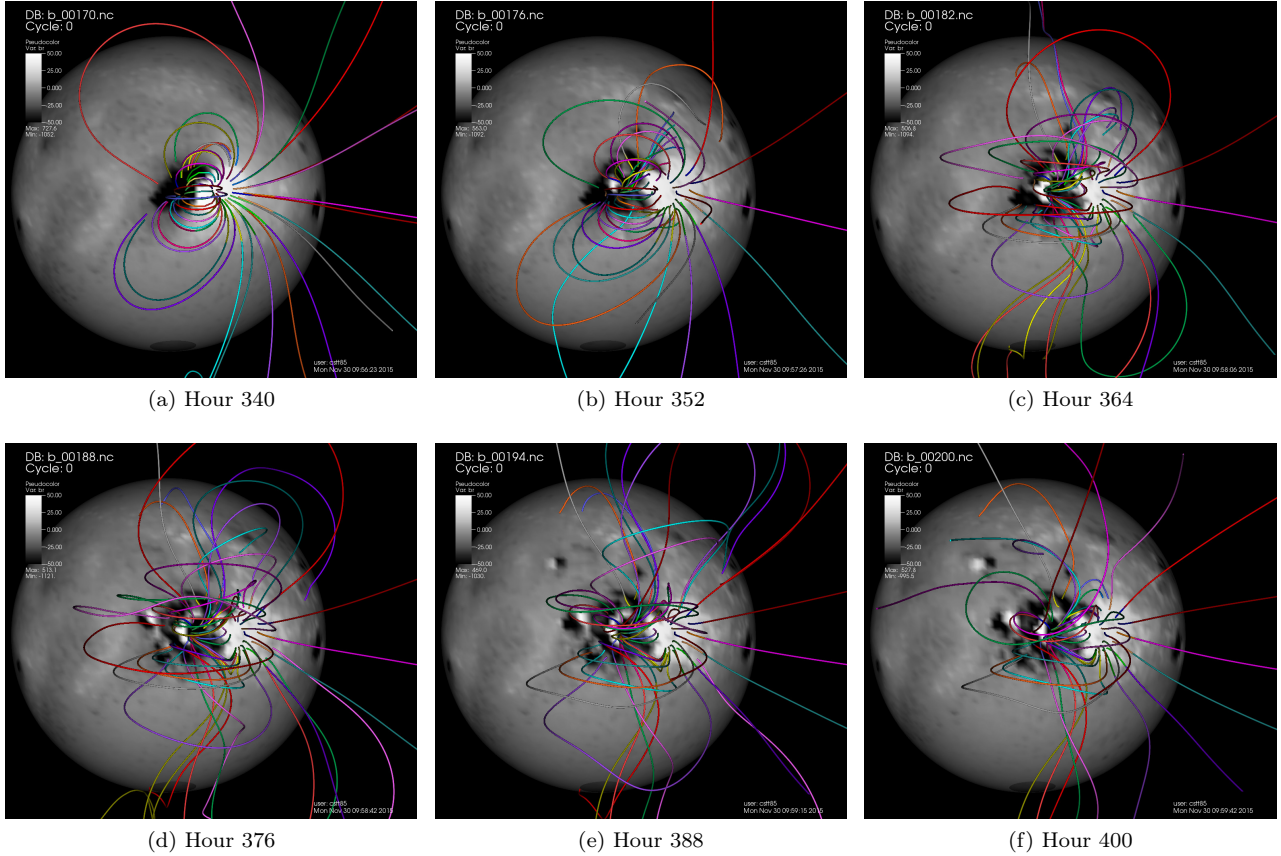
(c) Hour 364

(d) Hour 376

(e) Hour 388

(f) Hour 400

Fig. 13.— Example magnetic field lines (with random colors for identification) of AR12209 when it appears on the east limb in the improved-reconstruction ADAPT simulation. Due to the structural change in the active region the magnetic field lines rearrange and erupt.
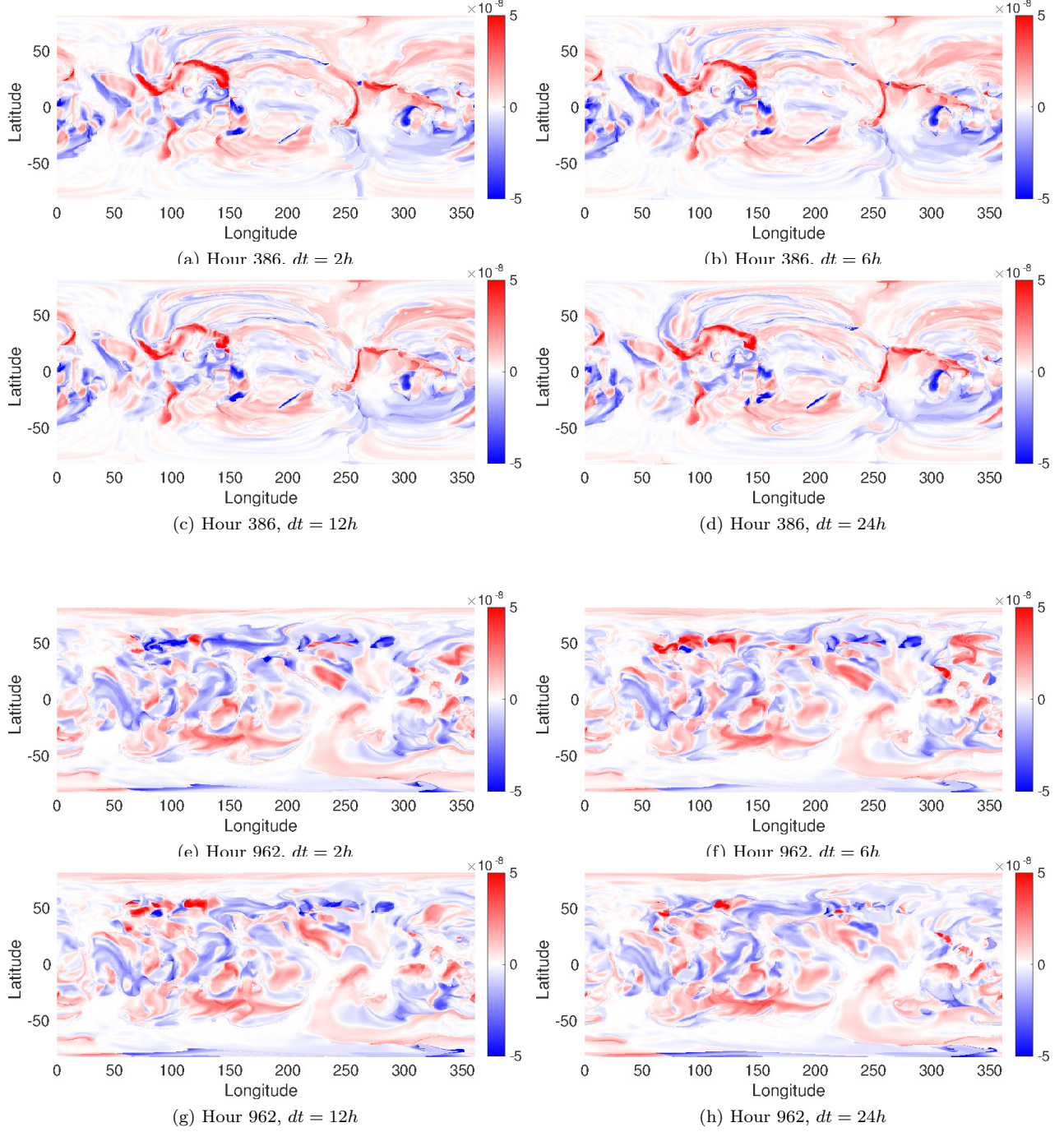
21

Fig. 14.— Current-helicity density α in the simulation domain in the improved-reconstruction ADAPT simulation for different values for dt and at two different times. Here α has been averaged along magnetic field lines, and is plotted on a sphere at height $r = 1.03327$. Units are m^{-1}.
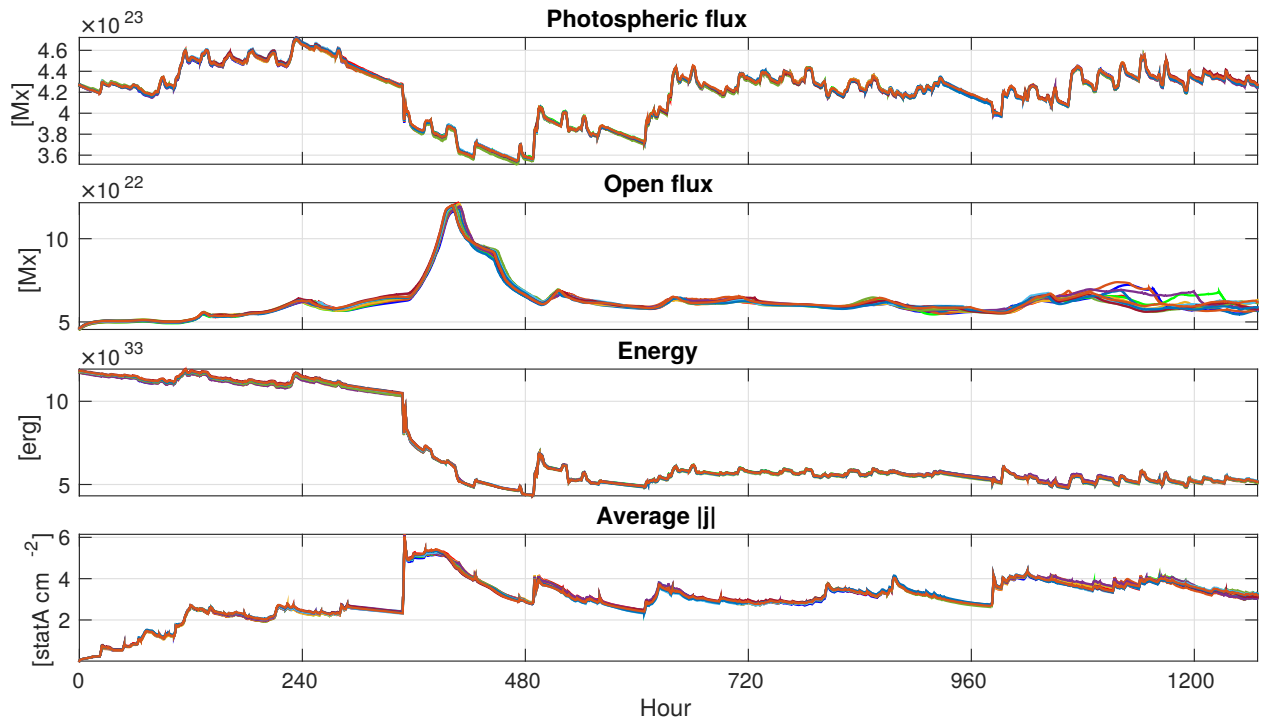
22

Fig. 16.— The same quantities as in Fig. 8 but for the twelve different members of the ADAPT ensemble (shown in different colors) in the improved-reconstruction case. All runs used $dt = 2h$.

A. NUMERICAL METHODS FOR POISSON EQUATIONS

A.1. Computational Coordinates

So far, we have used standard spherical coordinates notation for defining the equations to be solved in the simulation. Our computational grid, however, is curvilinear, and the computational coordinates (x, y, z) are defined in terms of (ϕ, θ, r) as in van Ballegooijen et al. (2000) by

$$x = \frac{\phi}{\Delta_\phi},$$

$$y = -\frac{\log(\tan(\theta/2))}{\Delta_\phi}$$

$$\text{and} \quad z = \frac{\log(r/R_\odot)}{\Delta_\phi},$$

where Δ_Φ is the azimuthal cell size (in radians) at the equator. The scale factors are given by $h_x = h_y = \Delta_\Phi r \sin(\theta)$ and $h_z = \Delta_r$. This grid is uniformly spaced in x, y and z, with cell-sizes increasing linearly with the radius. As we stay on the surface of the sphere for solving the Poisson equations 8 and 10, we only need a $2D$ Poisson solver. In Sec. A.2 we describe the solver we use in our simulation.

The poles are cut off at ± 81.7 degrees in order to avoid having to deal with the pole problem (see, e.g., Ronchi et al. (1996); Kageyama & Sato (2004)), and to avoid time-stepping restrictions due to the convergence of the cell sizes towards the poles. See Yeates (2014) for a possible solution by using a variable grid that doubles the cell size towards the pole. We are planning to integrate this into our simulation code.

Instead of solving the equations on the curvilinear grid defined by the above coordinates, we take a closer look at the stencil we receive from a finite volume discretization of Eq. 8 in curvilinear coordinates. With h_{ex} and h_{ey} the distances of the cell centres in horizontal and vertical direction and by using compass notation, we get

$$B_z(x, y) = -\frac{1}{h_x h_y} \begin{bmatrix} 0 & \frac{h_{ex}^N}{h_{ey}^N} & 0 \\ \frac{h_{ey}^W}{h_{ex}^W} & -\Sigma & \frac{h_{ey}^E}{h_{ex}^E} \\ 0 & \frac{h_{ex}^S}{h_{ey}^S} & 0 \end{bmatrix} \Phi(x, y),$$

with $\Sigma = h_{ex}^N/h_{ey}^N + h_{ey}^E/h_{ex}^E + h_{ex}^S/h_{ey}^S + h_{ex}^W/h_{ey}^W$. Due to the uniform spacing we can assume $h_{ex}^D = h_{ey}^D$ for $D \in \{N, E, S, W\}$, and therefore we get the standard Laplace five point stencil:

$$B_z = -\frac{1}{h_x h_y} \begin{bmatrix} 0 & 1 & 0 \\ 1 & -4 & 1 \\ 0 & 1 & 0 \end{bmatrix} \Phi(x, y).$$

By multiplying both sides of the equation by $h_x h_y$, the stencil becomes the one for the Cartesian grid. That means that by multiplying the righthand side of the Poisson equation by $h_x h_y = \Delta_\Phi^2 \sin^2(\theta)$ we can get Φ by solving the equation on a Cartesian grid.

Similarly, the discretized form of Eq. 10 in curvilinear coordinates can be solved on a Cartesian grid. In the next section, the benefit of doing so is demonstrated.

A.2. Poisson Solver

We have implemented a geometric multigrid solver (see, e.g. Trottenberg et al. (2001); Briggs et al. (2000) and references therein) which uses Red-Black Gauss-Seidel smoothing, weighted averaging as restriction and prolongation based on Taylor expansion (in order to preserve magnetic flux, see e.g., van der Holst & Keppens (2007)). Our simulation grid in this work is a 192×160 cell-centred grid and we coarsen down to 12×10, that

Table 1: Convergence of Multigrid Poisson solver

| | Curvilinear | | Cartesian | |
Cycle/BC	ρ_{mean}	#Iterations	ρ_{mean}	#Iterations
V(2, 1)/NM	*	*	0.44	30
F(2, 1)/NM	*	*	0.24	17
V(2, 1)/DIR	0.34	31	0.25	18
F(2, 1)/DIR	0.19	18	0.14	13

NOTE.—Convergence behaviour of the multigrid Poisson solver for stopping criterion $r_n \leq 1.0 \times 10^{-8}$, Neumann (NM) or Dirichlet (DIR) top and bottom boundaries and V or F cycles. An asterix refers to a stalled iteration ($\rho_{end} \approx 1$) before the stopping criterion was reached.

means we have five levels in the multigrid hierarchy. Horizontally, we apply periodic boundary conditions. On top and bottom, we have homogenous Neumann boundary conditions for solving Eq. 8 and homogenous Dirichlet for Eq. 10. We do F(2, 1) cycles, i.e., two pre- and one postsmoothing step. F cycles, as defined in Brandt (1984), are about as effective as W cycles, but they are less computationally expensive. The iteration is stopped when the residual $r_i = f - Au_i$ (with subscript i the iteration number, f the righthand side of the equation, A the system matrix and u_i the current approximation to the solution) is smaller than or equal to 1.0×10^{-8}.

For analysing the efficiency of the solver, we have a look at the convergence factor $\rho = r_{i+1}/r_i$, and its geometric mean $\rho_{mean} = \sqrt[n]{r_{end}/r_{start}}$, and we also consider V(2, 1) cycles. Tab. 1 shows how the solver performs for the multiple bipole simulation, both on the original curvilinear and on the Cartesian grid discussed in Sec. A.1. Results are shown both for the Neumann problem (inductive part of the electric field) and for the Dirichlet problem (non-inductive part), using the stopping criterion imposed in our simulation. One can observe that the cell-centred grid in combination with Neumann boundaries poses some challenges to the solver on the curvilinear grid, where the residual stalls at a certain level due to boundary effects. On a Cartesian grid, however, the solver shows reasonable performance for all setups. For the setup in our simulation, we reach the criterion after seventeen iteration steps with a mean convergence factor of 0.24 in the Neumann case, and $\rho_{mean} = 0.14$ after thirteen iteration steps in the Dirichlet case. In tests with different stopping criteria we observed that up to a relative stopping criterion of $r_n/r_{start} \leq 1.0 \times 10^{-6}$ the solver also converged on the curvilinear grid with Neumann boundaries.

REFERENCES

Amari, T., Luciani, J. F., Aly, J. J., Mikic, Z., & Linker, J. 2003, ApJ, 595, 1231

Antiochos, S. K. 2013, ApJ, 772, 72

Arge, C. N., Henney, C. J., Hernandez, I. G., et al. 2013, AIPC, 1539, 11

Arge, C. N., Henney, C. J., Koller, J., et al. 2010, 2010AIPC 1216, 1216, 343

Brandt, A. 1984, Multigrid Techniques: 1984 Guide with Applications to Fluid Dynamics, GMD-Studien

Briggs, W. L., Henson, V. E., & McCormick, S. F. 2000, A Multigrid Tutorial, 2nd edn. (SIAM)

Cheung, M. C. M., & DeRosa, M. L. 2012, ApJ, 757, 147

Edwards, S., Yeates, A., Bocquet, F.-X., & Mackay, D. 2015, Solar Phys., 290, 2791

Fisher, G., Welsch, B., & Abbett, W. 2012, Solar Phys., 277, 153

Fisher, G. H., Welsch, B. T., Abbett, W. P., & Bercik, D. J. 2010, ApJ, 715, 242

Gibb, G. P. S., Mackay, D. H., Green, L. M., & Meyer, K. A. 2014, ApJ, 782

Harvey, J. W., Hill, F., Hubbard, R. P., et al. 1996, Science, 272, 1284

Henney, C. J., Toussaint, W. A., White, S. M., & Arge, C. N. 2012, Space Weather, 10

Hickmann, K. S., Godinez, H. C., Henney, C. J., & Arge, C. N. 2015, Solar Phys., 290, 1105

Kageyama, A., & Sato, T. 2004, GGG, 5

Kazachenko, M. D., Fisher, G. H., & Welsch, B. T. 2014, ApJ, 795, 17

Knizhnik, K. J., Antiochos, S. K., & DeVore, C. R. 2015, ApJ, 809, 137

Mackay, D., & Yeates, A. 2012, Living Reviews in Solar Physics, 9, 6

Mackay, D. H. 2006, ApJ, 642, 1193

Mackay, D. H., DeVore, C. R., & Antiochos, S. K. 2014, ApJ, 784, 164

Mackay, D. H., Green, L. M., & van Ballegooijen, A. A. 2011, ApJ, 729, 97

Mackay, D. H., & van Ballegooijen, A. A. 2001, ApJ, 560, 445

—. 2005, ApJ, 621, L77

—. 2006, ApJ, 641, 577

Ronchi, C., Iacono, R., & Paolucci, P. S. 1996, J. Comp. Phys., 124, 93

Schrijver, C. J., & DeRosa, M. L. 2003, Solar Phys., 212, 165

Schüssler, M., & Baumann, I. 2006, A&A, 459, 945

Snodgrass, H. B. 1983, ApJ, 270, 288

Sun, X., Bobra, M. G., Hoeksema, J. T., et al. 2015, ApJL, 804, L28

Thalmann, J. K., Su, Y., Temmer, M., & Veronig, A. M. 2015, ApJL, 801, L23

Trottenberg, U., Oosterlee, C. W., & Schüller, A. 2001, Multigrid (San Diego, U.S.A.: Academic Press)

Upton, L., & Hathaway, D. H. 2014, ApJ, 780, 5

van Ballegooijen, A. A., Priest, E. R., & Mackay, D. H. 2000, ApJ, 539, 983

van der Holst, B., & Keppens, R. 2007, J. Comp. Phys., 226, 925

Worden, J., & Harvey, J. 2000, Solar Phys., 195, 247

Yang, L. P., Feng, X. S., Xiang, C. Q., et al. 2012, JGRA, 117

Yang, W. H., Sturrock, P. A., & Antiochos, S. K. 1986, ApJ, 309, 383

Yeates, A. R. 2014, Solar Phys., 289, 631

Yeates, A. R., & Mackay, D. H. 2012, ApJL, 753

Yeates, A. R., Mackay, D. H., & van Ballegooijen, A. A. 2007, Solar Phys., 245, 87

—. 2008, Solar Phys., 247, 103

Yeates, A. R., Mackay, D. H., van Ballegooijen,
A. A., & Constable, J. A. 2010, JGRA, 115,
9112